

# Epitaxy and transport properties of alkali-earth palladate thin films

Yusuke Kozuka, Taisuke T. Sasaki, Terumasa Tadano & Jun Fujioka

**To cite this article:** Yusuke Kozuka, Taisuke T. Sasaki, Terumasa Tadano & Jun Fujioka (2023) Epitaxy and transport properties of alkali-earth palladate thin films, Science and Technology of Advanced Materials, 24:1, 2265431, DOI: [10.1080/14686996.2023.2265431](https://doi.org/10.1080/14686996.2023.2265431)

**To link to this article:** <https://doi.org/10.1080/14686996.2023.2265431>



© 2023 The Author(s). Published by National Institute for Materials Science in partnership with Taylor & Francis Group.



Published online: 18 Oct 2023.



Submit your article to this journal [↗](#)



Article views: 440







View related articles [↗](#)



View Crossmark data [↗](#)

# Epitaxy and transport properties of alkali-earth palladate thin films

Yusuke Kozuka <sup>a</sup>, Taisuke T. Sasaki <sup>b</sup>, Terumasa Tadano <sup>b</sup> and Jun Fujioka <sup>c</sup>

<sup>a</sup>Research Center for Materials Nanoarchitectonics, National Institute for Materials Science (NIMS), Tsukuba, Japan;

<sup>b</sup>Research Center for Magnetic and Spintronic Materials, National Institute for Materials Science (NIMS), Tsukuba, Japan;

<sup>c</sup>Department of Material Science, University of Tsukuba, Tsukuba, Japan

## ABSTRACT

Topological insulators and semimetals are an interesting class of materials for new electronic and optical applications owing to their characteristic electromagnetic responses originating from the spin-orbit coupled band structures. However, topological electronic structures are rare in oxide materials despite their chemical stability being preferable for applications. In this study, given the theoretical prediction of Dirac bands in  $\text{CaPd}_3\text{O}_4$ , we investigate the fabrication and transport properties of  $\text{SrPd}_3\text{O}_4$  and  $\text{CaPd}_3\text{O}_4$  thin films as candidates of oxide Dirac semimetals. We have found that these materials are epitaxially grown on  $\text{MgO}$  (100) substrate under limited growth conditions by pulsed laser deposition. The transport properties show a weak temperature dependence, suggestive of narrow-gap properties, although unintentionally doped holes hinder us from revealing the presence of the Dirac band. Our study establishes the basic thermodynamics of thin-film fabrication of these materials and will lead to interesting properties characteristic of topological band structure by modulating the electronic structure by, for example, chemical substitutions or pressure.

## ARTICLE HISTORY

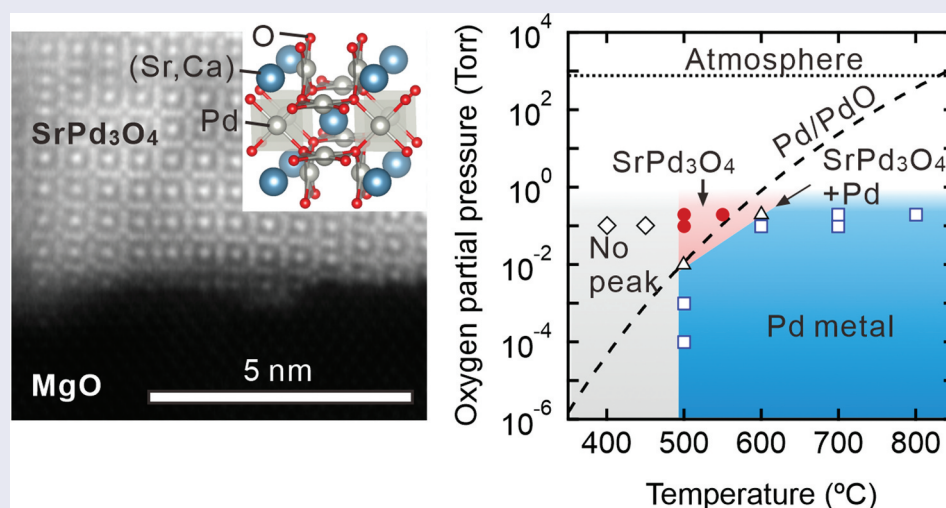
Received 21 June 2023

Revised 28 August 2023

Accepted 26 September 2023

## KEYWORDS

Palladate; thin film; transmission electron microscopy; first-principles calculation; transport properties



## IMPACT STATEMENT



We report the fabrication and transport properties of  $\text{NaPt}_3\text{O}_4$ -type alkali-earth palladate thin films for the first time, adding a new oxide narrow-gap material to the field of oxide electronics.

## 1. Introduction

Since the discovery of topological insulators and semimetals, a number of topological materials have been predicted and experimentally confirmed [1–5]. Topologically nontrivial band structures are realized when multiple bands with different symmetries are hybridized with each other, and therefore, narrow band-gap materials with strong spin–orbit interaction are straightforward choices. Along this guideline, pnictides

and chalcogenides containing heavy elements such as tellurides, antimonides, and bismuthides are representative candidates [2–4].

Beyond these standard topological materials, transition-metal oxides are an interesting class of materials as they possess a strong correlation as well. Among them, Ir oxides including perovskite and pyrochlore materials have been intensively studied because of the competing energy scales of electron correlation and

**CONTACT** Yusuke Kozuka  KOZUKA.Yusuke@nims.go.jp  Research Center for Materials Nanoarchitectonics, National Institute for Materials Science (NIMS), 1-1 Namiki, Tsukuba, Ibaraki 305-0044, Japan

© 2023 The Author(s). Published by National Institute for Materials Science in partnership with Taylor & Francis Group.

This is an Open Access article distributed under the terms of the Creative Commons Attribution License (<http://creativecommons.org/licenses/by/4.0/>), which permits unrestricted use, distribution, and reproduction in any medium, provided the original work is properly cited. The terms on which this article has been published allow the posting of the Accepted Manuscript in a repository by the author(s) or with their consent.

spin–orbit interaction, which leads to various topological phases [6–8] in response to environmental changes such as temperature, magnetic field, and pressure [9–12].

Utilizing thin-film techniques, the low-dimensional and interface properties have additionally been investigated, enabling the artificial design of correlated topological properties [13–15]. As one of the advantages of oxide thin films, the influences of epitaxial strain have been intensively studied for perovskite oxides owing to their flexibility on the lattice and the variety of the choice of substrates [16]. As a result, structural changes such as  $MO_6$  ( $M$ : transition metal) octahedral rotations or lattice compression/elongation have been utilized to drastically alter the electronic structure via the modulations of band width as well as underlying crystal symmetry, causing, for example, the carrier-type change, or mobility enhancement in zero-gap or narrow-gap oxides [17,18]. Despite such intriguing possibilities, however, the thin films of topological transition-metal oxides are rarely studied other than Iridates [17] or Niobates [18].

Palladium oxides are thought to be other candidates for topological materials as some of them have been predicted to involve narrow or zero band gaps by first-principles calculations [19–21]. Experimentally, the bulk properties of some of the palladates have been investigated, and zero-gap or narrow-gap properties have been revealed [22–24]. In contrast, palladate thin films have been scarcely fabricated except for a few examples such as  $PbPdO_2$  (Refs. [25–31]). Here, we report the fabrication of  $APd_3O_4$  thin films ( $A$ : Ca or Sr) and their transport properties, which have not been achieved so far. This class of materials possesses a  $NaPt_3O_4$ -type crystal structure [32], where square planar-coordinated Pd plaquettes are stacked along all three crystallographic directions as shown in Figure 1 [33].

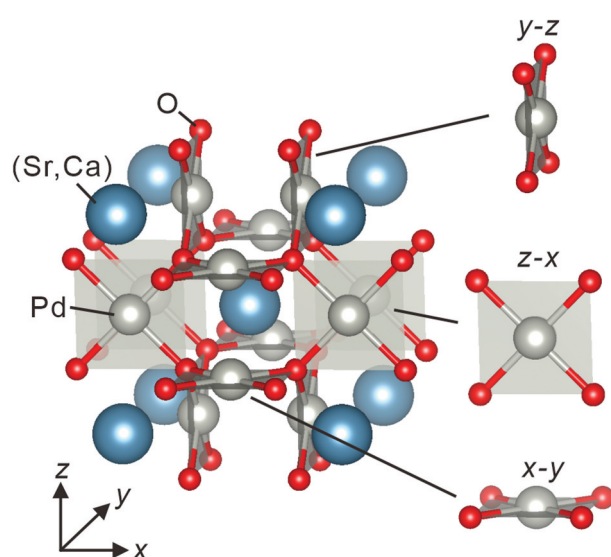


**Figure 1.** The crystal structure of  $SrPd_3O_4$  and  $CaPd_3O_4$  produced by VESTA [33]. Square planar-coordinated  $PdO_4$  plaquettes are stacked along all three crystallographic directions.

Unlike perovskite-type oxides, it is still not clear whether strain engineering is feasible in  $NaPt_3O_4$ -type materials due to the lack of studies of thin-film fabrication.

In this study, we find that  $APd_3O_4$  thin films can be epitaxially grown on  $MgO$  (100) substrate under limited growth conditions by pulsed laser deposition, while a single phase is not obtained for other typical oxide substrates such as  $SrTiO_3$  or  $MgAl_2O_4$  within our investigation. The electrical transport measurements show that  $CaPd_3O_4$  thin film is weakly insulating, whereas  $SrPd_3O_4$  thin film is metallic with a slight upturn at low temperatures, suggestive of proximity to band gap closing. First-principles band calculation also supports narrow-gap properties of  $CaPd_3O_4$  and  $SrPd_3O_4$ . Our study indicates that these compounds would be promising candidates as new topological materials by appropriate chemical substitution or by external stimuli such as pressure.

## 2. Experimental details

$APd_3O_4$  thin films are grown by pulsed laser deposition using the fourth harmonic wave of the Nd:YAG (LS-2145TF, LOTIS TII, Belarus) laser with a typical laser energy of 20 mJ/pulse. The targets are made by the solid-state reaction of  $ACO_3$  and  $PdO$  powder at a molar ratio of 1:3 at 1200°C for 24 h in the air. We have employed  $MgO$  (100) ( $a = 4.21$  Å) and  $MgAl_2O_4$  ( $a = 8.08$  Å,  $a/2 = 4.04$  Å) substrates because of their bulk lattice constants close to  $SrPd_3O_4$  ( $a = 5.83$  Å,  $a/\sqrt{2} = 4.12$  Å) and  $CaPd_3O_4$  ( $a = 5.75$  Å,  $a/\sqrt{2} = 4.06$  Å) when the lattice is rotated by 45° around the out-of-plane axis. We have also tried  $SrTiO_3$  ( $a = 3.91$  Å) and  $GdScO_3$  ( $a = 5.54$  Å,  $b = 5.71$  Å,  $c = 7.93$  Å,  $a_{\text{pseudo}} = \sqrt{(2a^2 + 2b^2 + c^2)/12} = 3.96$  Å) substrates for comparison. The crystal structure and film quality are characterized by X-ray diffraction (SmartLab, Rigaku Co., Japan) and (scanning) transmission electron microscope ((S)TEM) (Titan G2 80-200, Thermo Fisher Scientific, USA). Thin-lamella specimens for the cross-sectional (S)TEM observation were prepared using a focused ion beam (FIB) (Helios G4 UX, Thermo Fisher Scientific, USA). Transport properties are measured by a standard four-probe method using a cryostat equipped with a 14 T superconducting magnet (PPMS DynaCool, Quantum Design, USA). Electrical contacts are made by ultrasonically binding the Al wires on the surface of the samples. We have used an excitation current of 1  $\mu A$ , while we have confirmed that the resistivity is not affected by the current at least between 0.1 and 100  $\mu A$ .

The band structures are calculated based on density functional theory using the *Vienna ab-initio simulation package* (VASP) [34], which

implements the projector augmented wave (PAW) method [35] with including the spin-orbit coupling. The plane-wave kinetic energy cutoff was set to 400 eV, and  $6 \times 6 \times 6$   $\Gamma$ -centred  $k$  points were used for the Brillouin zone integration. The Heyd-Scuseria-Ernzerhof (HSE06) screened hybrid functional is used [36–38].

### 3. Thin film growth and structural and chemical characterization

The optimization of the thin-film growth of  $\text{SrPd}_3\text{O}_4$  on  $\text{MgO}$  (100) substrate is summarized in Figure 2(a), where substrate temperature and oxygen partial pressure are varied as typical thermodynamic variables. Here, the phases are determined from the peak positions of X-ray diffraction as some of the typical diffraction patterns shown in Figure 2(b). At temperatures lower than  $500^\circ\text{C}$ , no indication of crystal phases is observed irrespective of the oxygen partial pressure, probably due to the low thermal energy for crystallization. On the other hand, the Pd metal is segregated at high temperatures above  $600^\circ\text{C}$ . The single phase of  $\text{SrPd}_3\text{O}_4$  thin films is obtained only around  $500^\circ\text{C}$  above 0.2 Torr oxygen partial pressure. Small Pd metal peaks sometimes remain in the X-ray diffraction, which is diminished by annealing at  $800^\circ\text{C}$  in a flowing oxygen atmosphere. This phase diagram is understood based on the Ellingham diagram of the phase equilibrium curve of Pd/PdO calculated from the Gibbs free energy for bulk as indicated by the dashed curve in Figure 2(a) [39]. This tendency contrasts with the case of many oxides, where thin films are frequently stabilized at much wider growth conditions than those of the bulk

when grown on an isostructural substrate as termed ‘epitaxial stabilization’ [40].

We also try growing  $\text{SrPd}_3\text{O}_4$  thin films on various substrates other than  $\text{MgO}$  (100) as shown in the X-ray diffraction patterns in Figure 2(c) but find that  $\text{SrPd}_3\text{O}_4$  films are not epitaxially grown on  $\text{MgAl}_2\text{O}_4$  (100),  $\text{SrTiO}_3$  (100),  $\text{GdScO}_3$  (110) substrates, while small  $\text{SrPd}_3\text{O}_4$  (111) peaks are seen in the case of  $\text{SrTiO}_3$  (100) substrate. In a sense, this is a surprising result because the lattice constant of  $\text{MgAl}_2\text{O}_4$  is better matched with  $\text{SrPd}_3\text{O}_4$  than that of  $\text{MgO}$ , which will be discussed later together with the results of TEM.

The crystal quality (mosaicity) of the  $\text{SrPd}_3\text{O}_4$  film grown on  $\text{MgO}$  (100) substrate is evaluated by the full-width at half-maximum of the rocking curve around the  $\text{SrPd}_3\text{O}_4$  (200) peak, which is  $2.54^\circ$  as shown in Figure 3(a). This value indicates a moderate crystal quality with a relatively large distribution of grain orientations. The epitaxial relationship is confirmed by reciprocal space mapping (Figure 3(b)) and pole figures (Figure 3(c)). These measurements show the [100] axis of the  $\text{SrPd}_3\text{O}_4$  film is along the [110] direction of the  $\text{MgO}$  substrate for better lattice matching. The pole figure clearly shows the four-fold symmetry of the  $\text{SrPd}_3\text{O}_4$  film. We have also investigated the growth of  $\text{CaPd}_3\text{O}_4$  films and found almost the same tendency as  $\text{SrPd}_3\text{O}_4$ . The lattice constants of  $\text{SrPd}_3\text{O}_4$  and  $\text{CaPd}_3\text{O}_4$  thin films are extracted from the reciprocal space mapping as  $5.78 \text{ \AA}$  (in-plane) and  $5.91 \text{ \AA}$  (out-of-plane) for  $\text{SrPd}_3\text{O}_4$  and  $5.75 \text{ \AA}$  (in-plane) and  $5.72 \text{ \AA}$  (out-of-plane) for  $\text{CaPd}_3\text{O}_4$ .

To further obtain insight, the microstructure is analyzed by cross-sectional TEM observation. Figure 4(a) shows a bright-field TEM image of

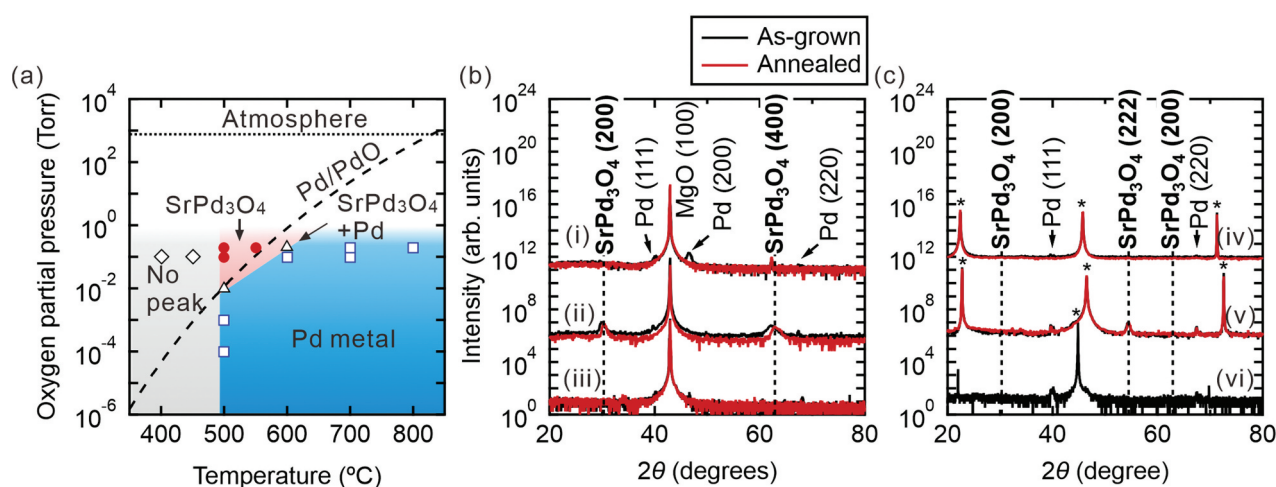


**Figure 2.** (a) Phase stability of  $\text{SrPd}_3\text{O}_4$  thin film grown by pulsed laser deposition on  $\text{MgO}$  (100) substrate as functions of growth temperature ( $T_g$ ) and oxygen partial pressure ( $P_{\text{O}_2}$ ). The phase equilibrium curve of Pd/PdO is also shown as a guide. (b)  $\theta$ - $2\theta$  scan of X-ray diffraction of  $\text{SrPd}_3\text{O}_4$  thin films under different growth conditions: (i)  $T_g = 700^\circ\text{C}$ ,  $P_{\text{O}_2} = 0.2$  Torr, (ii)  $T_g = 500^\circ\text{C}$ ,  $P_{\text{O}_2} = 0.2$  Torr, (iii)  $T_g = 450^\circ\text{C}$ ,  $P_{\text{O}_2} = 0.1$  Torr. (c) X-ray diffraction of  $\text{SrPd}_3\text{O}_4$  thin films grown on different substrates at  $500^\circ\text{C}$  under 0.2 Torr: (iv)  $\text{GdScO}_3$  (110) substrate, (v)  $\text{SrTiO}_3$  (100) substrate, (vi)  $\text{MgAl}_2\text{O}_4$  (100) substrate. Asterisks in (c) indicate the peaks of substrates. In (b) and (c), black and red curves are the data of as-grown films and the films annealed at  $800^\circ\text{C}$  in the air for 12 hours, respectively. The data of X-ray diffraction are shifted vertically for clarity.



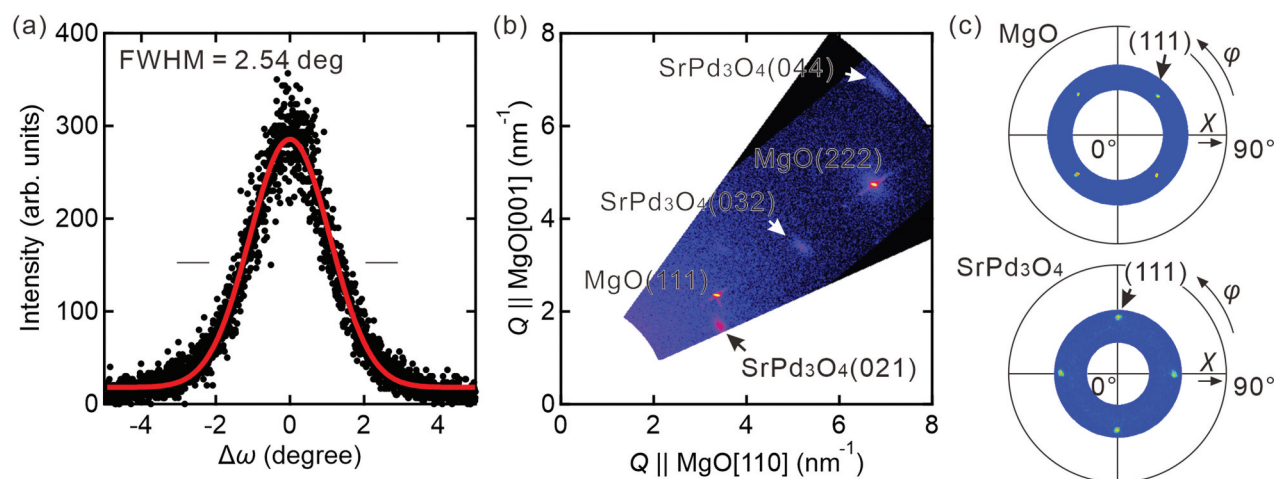


**Figure 3.** (a) Rocking curve around the  $\text{SrPd}_3\text{O}_4$  (200) peak, (b) Reciprocal space mapping, and (c) Pole figure. In (c), The pole figure of the MgO substrate is also shown to clarify the in-plane relationship between the film and the substrate.

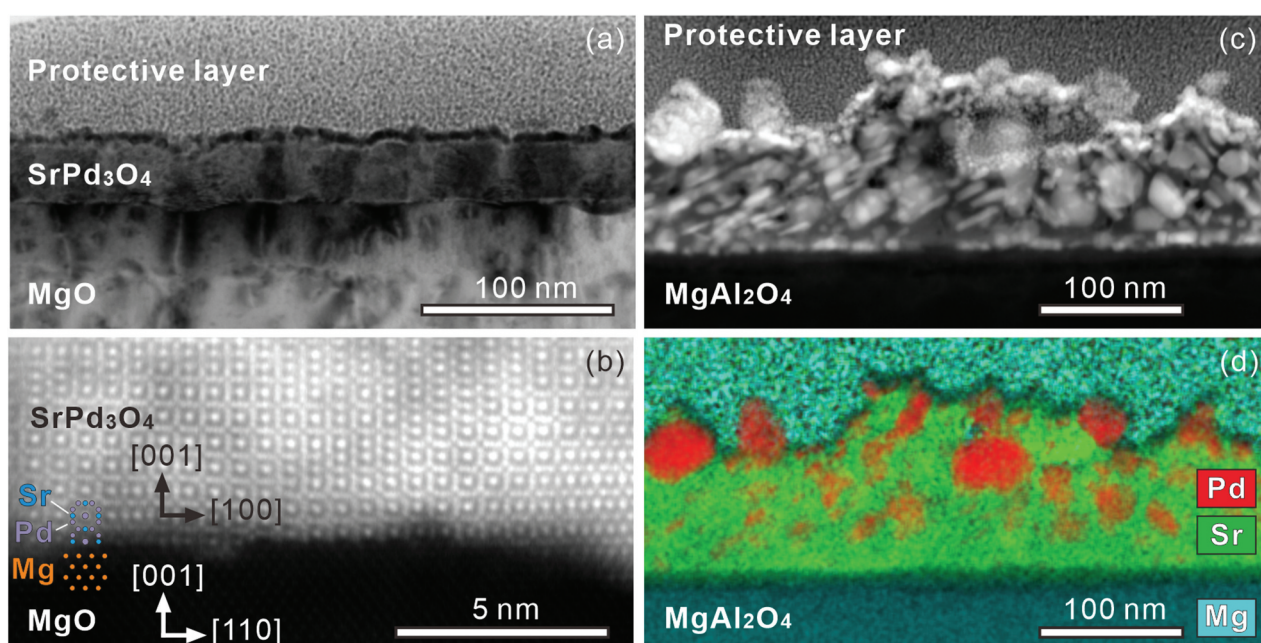


**Figure 4.** (a) A bright-field transmission electron microscope image and (b) a high-magnification HAADF-STEM image of a  $\text{SrPd}_3\text{O}_4$  film grown on MgO (100) substrate. (c) A low-magnification HAADF-STEM image and (d) an EDS map of a  $\text{SrPd}_3\text{O}_4$  film grown on  $\text{MgAl}_2\text{O}_4$  (100) substrate.

a  $\text{SrPd}_3\text{O}_4$  thin film grown on a MgO (100) substrate, where columnar growth of the  $\text{SrPd}_3\text{O}_4$  layer is clearly visible due to the different diffraction contrasts. A high-magnification high-angle annular dark field STEM (HAADF-STEM) image in Figure 4(b) shows, as found by X-ray diffraction, (100)-oriented epitaxial growth is confirmed. In contrast to the  $\text{SrPd}_3\text{O}_4$  layer grown on the MgO substrate, a low-magnification HAADF-STEM image in Figure 4(c) indicates the occurrence of the phase separation within the  $\text{SrPd}_3\text{O}_4$  layer grown on the  $\text{MgAl}_2\text{O}_4$  substrate. The elemental mapping by energy-dispersive X-ray spectroscopy (EDS) in Figure 4(d) indicates that the  $\text{SrPd}_3\text{O}_4$  layer phase-separates into Pd metal and  $\text{SrO}_x$ .

The chemical compositions of  $\text{SrPd}_3\text{O}_4$  and  $\text{CaPd}_3\text{O}_4$  films grown on MgO (100) substrates are

characterized by EDS mapping as shown in Figure 5. We find that all the elements are almost uniformly distributed within the films without significant segregation. For  $\text{CaPd}_3\text{O}_4$  thin film, the cation ratio is nearly  $\text{Pd}/\text{Ca} \approx 3$ , consistent with the designed composition, whereas  $\text{Pd}/\text{Sr} \approx 2$  in the case of  $\text{SrPd}_3\text{O}_4$  thin film. The deviation from the designed composition of  $\text{SrPd}_3\text{O}_4$  film may be due to incongruent ablation of pulsed laser between Sr and Pd.

#### 4. Discussions on thin film growth

The failure of the epitaxial growth of  $\text{SrPd}_3\text{O}_4$  on  $\text{MgAl}_2\text{O}_4$  may be understood by the difference between the atomic arrangements of MgO and  $\text{MgAl}_2\text{O}_4$  shown in Figure 6 [33]. In the cases of  $\text{SrPd}_3\text{O}_4$  and MgO, oxide

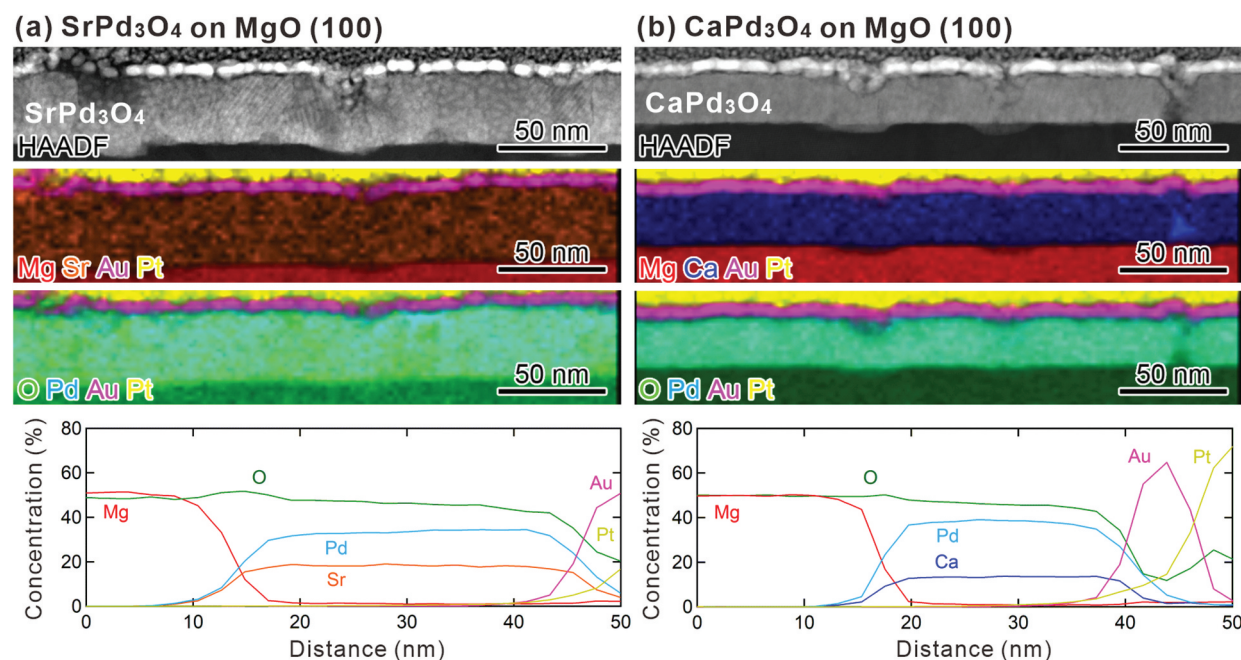


**Figure 5.** HAADF-STEM images, EDS maps, and line scans of the EDS maps for (a)  $\text{SrPd}_3\text{O}_4$  and (b)  $\text{CaPd}_3\text{O}_4$  films grown on  $\text{MgO}$  (100) substrates. Au and Pt layers on the films are the protective layers deposited for the TEM specimen fabrication.

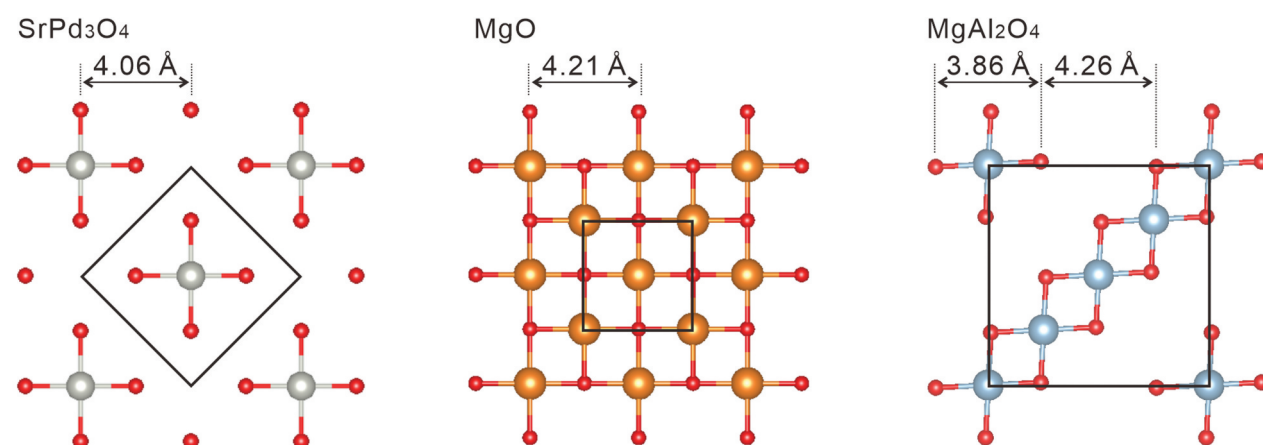


**Figure 6.** Surface atomic arrangements of  $\text{SrPd}_3\text{O}_4$ ,  $\text{MgO}$ , and  $\text{MgAl}_2\text{O}_4$ . The black squares indicate the unit cells projected along the  $c$ -axis.

ions are equally spaced with a lattice mismatch of 2.1%, whereas the arrangement of the oxide ions is distorted from the square lattice for  $\text{MgAl}_2\text{O}_4$ . We speculate that the three-dimensional  $\text{PdO}_4$  chains of the  $\text{NaPt}_3\text{O}_4$ -type lattice may not be flexible enough to accommodate the unevenly spaced atomic arrangement of the  $\text{MgAl}_2\text{O}_4$  surface lattice, leading to the unstable formation of  $\text{SrPd}_3\text{O}_4$ . The stiffness of the  $\text{NaPt}_3\text{O}_4$ -type crystal structure has also been pointed out in Ref. [41] in connection with the absence of structural transitions even with the one-dimensional chains composed of  $\text{Pd } dz^2$  orbitals, where Peierls transition is expected. This situation is contrasted with perovskite or rutile structures composed of  $\text{MO}_6$  ( $M$ : transition metal) octahedral networks, where the freedom of the octahedral rotation gives the flexibility to adapt the lattice to an isostructural substrate [42,43]

even with a relatively large lattice mismatch over  $\sim 3\%$  [44]. Thus, given this thought,  $\text{NaPt}_3\text{O}_4$ -type materials may not exhibit such a high controllability of electronic structure by epitaxial strain, unlike perovskite materials.

## 5. Electrical transport

We have measured the electrical transport of the  $\text{SrPd}_3\text{O}_4$  and  $\text{CaPd}_3\text{O}_4$  thin films as shown in Figure 7 for annealed samples. The  $\text{CaPd}_3\text{O}_4$  thin film is weakly insulating, while  $\text{SrPd}_3\text{O}_4$  thin film is metallic down to low temperature with a slight upturn below 10 K. Carrier density and mobility are also estimated from the Hall effect, which is in the order of  $10^{21} \text{ cm}^{-3}$  (hole-type) and  $1 \text{ cm}^2 \text{ V}^{-1} \text{ s}^{-1}$ , respectively, in both



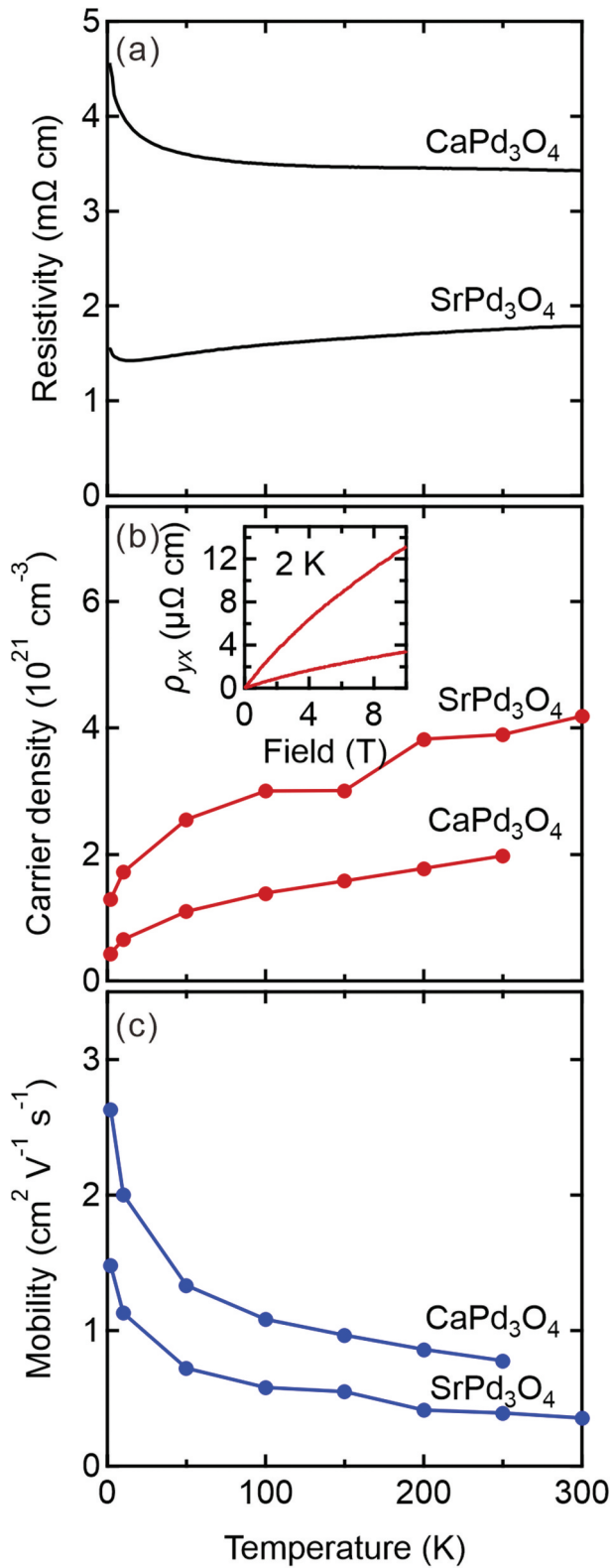


**Figure 7.** Temperature dependence of (a) resistivity, (b) carrier density, and (c) mobility of SrPd<sub>3</sub>O<sub>4</sub> and CaPd<sub>3</sub>O<sub>4</sub> thin films grown on MgO (100) substrate at 500°C under 0.2 Torr followed by annealing in air at 800°C. The carrier type measured from the Hall effect is *p*-type for both samples as shown in the inset of the panel (b).

compounds. The carrier density of the thin films is about one order of magnitude larger than the previously reported values for bulk [23,24] probably due to non-stoichiometry introduced in the

growth process. The temperature dependence data show that the carrier density decreases and the mobility gradually increases with decreasing temperature as typical behavior of a narrow-gap semiconductor. The mobility, although not specified in the previous reports, is comparable to the bulk value, if estimated from the resistivity and Hall coefficient.

## 6. Band calculations

To understand the electrical transport, we have carried out first-principles calculation. Since the band calculation with the generalized gradient approximation (GGA) for the exchange-correlation functional often underestimate the band gap of semiconductors, the previous theoretical study on CaPd<sub>3</sub>O<sub>4</sub> employed modified Becke-Johnson (mBJ) meta-GGA functional [45] for the better estimation [46] and reported Dirac-type band crossings [20]. In this study, however, we have employed the HSE06 screened hybrid functional as a recent study shows that this functional qualitatively reproduces a small band gap observed for bulk CaPd<sub>3</sub>O<sub>4</sub> [47].

Figure 8 shows the band calculation for SrPd<sub>3</sub>O<sub>4</sub> and CaPd<sub>3</sub>O<sub>4</sub> using lattice parameters estimated from the reciprocal space mapping. We find the band gaps open between the crystal field split bands between the *d*<sub>x<sup>2</sup>-y<sup>2</sup> and *d*<sub>z<sup>2</sup> orbitals. The values of the band gaps are 0.22 eV and 0.27 eV for SrPd<sub>3</sub>O<sub>4</sub> and CaPd<sub>3</sub>O<sub>4</sub>, respectively [48]. We have also confirmed that the band structures in Figure 8 are not significantly different from those obtained using bulk lattice parameters [20] although the band gap of SrPd<sub>3</sub>O<sub>4</sub> is slightly reduced by ~0.02 eV when the experimental lattice constants of the</sub></sub>

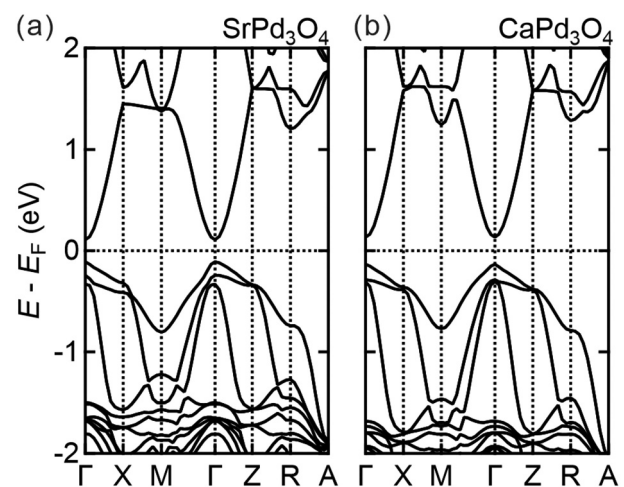


**Figure 8.** First-principles band calculations of (a) SrPd<sub>3</sub>O<sub>4</sub> and (b) CaPd<sub>3</sub>O<sub>4</sub> using lattice parameters extracted from the reciprocal space mapping. The calculated band gaps are 0.22 eV and 0.27 eV for SrPd<sub>3</sub>O<sub>4</sub> and CaPd<sub>3</sub>O<sub>4</sub>, respectively.

APd<sub>3</sub>O<sub>4</sub> films grown on MgO substrate are used, compared with that calculated with the bulk lattice constant. This small variation of the band gap by strain indicates that it may be difficult to utilize epitaxial strain to drastically modulate the electronic structure in the case of NaPt<sub>3</sub>O<sub>4</sub>-type materials due to the inflexibility of the lattice in contrast to the case of perovskite materials, which can accommodate a large variation of strains by MO<sub>6</sub> octahedral rotations as introduced above. Instead, the substitution of the A-site may work more effectively to control the band gap for APd<sub>3</sub>O<sub>4</sub> through crystal field splitting between  $d_{x^2-y^2}$  and  $d_{z^2}$ .

In light of a recent experimental study, the value of the band gap for CaPd<sub>3</sub>O<sub>4</sub> using HSE06 screened hybrid functional seems to be overestimated compared with that obtained from the optical spectroscopy, which is ~0.12 eV [47]. The band gap of SrPd<sub>3</sub>O<sub>4</sub> is expected to be even smaller, close to band touching. Unfortunately, we cannot assess whether our films are Dirac semimetals, as suggested in Ref. [20] or narrow-gap semiconductors as in the bulk based on the transport data in Figure 7 due to a large number of extrinsic carriers. We have also tried to estimate the band gaps of our CaPd<sub>3</sub>O<sub>4</sub> and SrPd<sub>3</sub>O<sub>4</sub> films by optical spectroscopy but failed due to residual carriers causing large Burstein-Moss shifts and Drude peaks, which awaits the improvements of the film quality in the future.

## 7. Conclusion

In this study, we report the fabrication of SrPd<sub>3</sub>O<sub>4</sub> and CaPd<sub>3</sub>O<sub>4</sub> thin films by pulsed laser deposition together with structural and transport properties. X-ray diffraction and transmission electron microscopy have revealed that (100)-oriented thin films are grown on MgO (100) substrates under limited growth conditions following the thermodynamic-phase diagram of Pd oxides, whereas other substrates including SrTiO<sub>3</sub>, GdScO<sub>3</sub>, MgAl<sub>2</sub>O<sub>4</sub> do not lead to clear crystallization within our investigation probably due to the inflexibility of the NaPt<sub>3</sub>O<sub>4</sub>-type crystal structure. The transport properties show a weak temperature dependence, suggestive of a narrow-gap semiconductor. However, a large number of extrinsic carriers are present in our films, which hinders us from accessing the properties originating from the possible topological bands. The first-principles band calculations show that these compounds may be narrow-gap semiconductors close to the topological-phase transition. The thin-film fabrication reported here will open a way to modulate the electronic structure by, for example, chemical substitution or pressure, which leads to a topological band structure.

## Acknowledgments

We acknowledge A. Kurita for the technical assistance with thin-film growth.

## Disclosure statement

No potential conflict of interest was reported by the author(s).

## Funding

This work was supported by Grants-in-Aid for Scientific Research (B) [Grant Number: 19H02604, 21K18813, and 22H01177], by Nippon Sheet Glass Foundation for Materials Science and Engineering, Japan, and by JST FOREST Program [Grant Number: JPMJFR203D]. MANA is supported by the World Premier International Research Center Initiative (WPI), MEXT, Japan.

## ORCID

Yusuke Kozuka  <http://orcid.org/0000-0001-7674-600X>  
Taisuke T. Sasaki  <http://orcid.org/0000-0002-5952-7638>  
Terumasa Tadano  <http://orcid.org/0000-0002-8132-2161>  
Jun Fujioka  <http://orcid.org/0000-0003-1340-0268>

## References

- [1] Kane CL, Mele EJZ. Z<sub>2</sub> topological order and the quantum spin Hall effect. *Phys Rev Lett.* 2005;95(14):146802. doi: 10.1103/PhysRevLett.95.146802
- [2] König M, Wiedmann S, Brüne C, et al. Quantum spin Hall insulator state in HgTe quantum wells. *Science.* 2007;318(5851):766–700. doi: 10.1126/science.1148047
- [3] Hsieh D, Qian D, Wray L, et al. A topological Dirac insulator in a quantum spin Hall phase. *Nature.* 2008;452(7190):970–974. doi: 10.1038/nature06843
- [4] Liu ZK, Zhou B, Zhang Y, et al. Discovery of a three-dimensional topological Dirac semimetal, Na<sub>3</sub>Bi. *Science.* 2014;343(6173):864–867. doi: 10.1126/science.1245085
- [5] Lv BQ, Weng HM, Weng BB, et al. Experimental discovery of Weyl semimetal TaAs. *Phys Rev X.* 2015;5(3):031013. doi: 10.1103/PhysRevX.5.031013
- [6] Pesin D, Balents L. Mott physics and band topology in materials with strong spin-orbit interaction. *Nat Phys.* 2010;6(5):376–381. doi: 10.1038/nphys1606
- [7] Kim BJ, Jin H, Moon SJ, et al. Novel  $J_{\text{eff}} = 1/2$  Mott state induced by relativistic spin-orbit coupling in Sr<sub>2</sub>IrO<sub>4</sub>. *Phys Rev Lett.* 2008;101(7):076402. doi: 10.1103/PhysRevLett.101.076402
- [8] Wang X, Turner AM, Vishwanath A, et al. Topological semimetal and fermi-arc surface states in the electronic structure of pyrochlore iridates. *Phys Rev B.* 2011;83(20):205101. doi: 10.1103/PhysRevB.83.205101
- [9] Ueda K, Fujioka J, Yang BJ, et al. Magnetic field-induced insulator-semimetal transition in a pyrochlore Nd<sub>2</sub>Ir<sub>2</sub>O<sub>7</sub>. *Phys Rev Lett.* 2015;115(5):056402. doi: 10.1103/PhysRevLett.115.056402
- [10] Ueda K, Oh T, Yang BJ, et al. Magnetic-field induced multiple topological phases in pyrochlore iridates with Mott criticality. *Nat Commun.* 2017;8(1):15515. doi: 10.1038/ncomms15515



- [11] Yamada R, Fujioka J, Kawamura M, et al. Large variation of Dirac semimetal state in perovskite  $\text{CaIrO}_3$  with pressure-tuning of electron correlation. *Phys Rev Lett.* 2019;123(21):216601. doi: [10.1103/PhysRevLett.123.216601](https://doi.org/10.1103/PhysRevLett.123.216601)
- [12] Fujioka J, Yamada R, Kawamura M, et al. Strong-correlation induced high-mobility electrons in Dirac semimetal of perovskite oxide. *Nat Commun.* 2019;10(1):362. doi: [10.1038/s41467-018-08149-y](https://doi.org/10.1038/s41467-018-08149-y)
- [13] Matsuno J, Ihara K, Yamamura S, et al. Engineering a spin-orbital magnetic insulator by tailoring superlattices. *Phys Rev Lett.* 2015;114(24):247209. doi: [10.1103/PhysRevLett.114.247209](https://doi.org/10.1103/PhysRevLett.114.247209)
- [14] Fujita TC, Kozuka Y, Uchida M, et al. Odd-parity magnetoresistance in pyrochlore iridate thin films with broken time-reversal symmetry. *Sci Rep.* 2015;5(1):9711. doi: [10.1038/srep09711](https://doi.org/10.1038/srep09711)
- [15] Kim WJ, Oh T, Song J, et al. Strain engineering of the magnetic multipole moments and anomalous Hall effect in pyrochlore iridate thin films. *Sci Adv.* 2020;6(20):eabb1539. doi: [10.1126/sciadv.abb1539](https://doi.org/10.1126/sciadv.abb1539)
- [16] Schlom DG, Chen LQ, Fennie CJ, et al. Elastic strain engineering of ferroic oxides. *MRS Bull.* 2014;39(2):118. doi: [10.1557/mrs.2014.1](https://doi.org/10.1557/mrs.2014.1)
- [17] Masuko M, Fujioka J, Nakamura M, et al. Strain-engineering of charge transport in the correlated Dirac semimetal of perovskite  $\text{CaIrO}_3$  thin films. *APL Mater.* 2019;7(8):081115. doi: [10.1063/1.5109582](https://doi.org/10.1063/1.5109582)
- [18] Ok JM, Mohanta N, Zhang J, et al. Correlated oxide Dirac semimetal in the extreme quantum limit. *Sci Adv.* 2021;7(38):eabf9631. doi: [10.1126/sciadv.abf9631](https://doi.org/10.1126/sciadv.abf9631)
- [19] Wang XL. Proposal for a new class of materials: spin gapless semiconductors. *Phys Rev Lett.* 2008;100(15):156404. doi: [10.1103/PhysRevLett.100.156404](https://doi.org/10.1103/PhysRevLett.100.156404)
- [20] Li G, Yan B, Wang Z, et al. Topological Dirac semimetal phase in Pd and Pt oxides. *Phys Rev B.* 2017;95(3):035102. doi: [10.1103/PhysRevB.95.035102](https://doi.org/10.1103/PhysRevB.95.035102)
- [21] Teicher SML, Lamontagne LK, Schoop LM, et al. Fermi-level Dirac crossings in  $4d$  and  $5d$  cubic metal oxides:  $\text{NaPd}_3\text{O}_4$  and  $\text{NaPt}_3\text{O}_4$ . *Phys Rev B.* 2019;99(19):195148. doi: [10.1103/PhysRevB.99.195148](https://doi.org/10.1103/PhysRevB.99.195148)
- [22] Itoh K, Yano Y, Tsuda N. Metal to insulator transition for  $\text{Ca}_{1-x}\text{Na}_x\text{Pd}_3\text{O}_4$ . *J Phys Soc Jpn.* 1999;68(9):3022–3026. doi: [10.1143/JPSJ.68.3022](https://doi.org/10.1143/JPSJ.68.3022)
- [23] Ichikawa S, Terasaki I. Metal-insulator transition in  $\text{Ca}_{1-x}\text{Li}_x\text{Pd}_3\text{O}_4$ . *Phys Rev B.* 2003;68(23):233101. doi: [10.1103/PhysRevB.68.233101](https://doi.org/10.1103/PhysRevB.68.233101)
- [24] Taniguchi T, Nagata Y, Ozawa TC, et al. Insulator-metal transition induced in  $\text{Sr}_{1-x}\text{Na}_x\text{Pd}_3\text{O}_4$  for small Na-substitutions. *J Alloys Compd.* 2004;373(1–2):67–72. doi: [10.1016/j.jallcom.2003.11.004](https://doi.org/10.1016/j.jallcom.2003.11.004)
- [25] Wang X, Peleckis G, Zhang C, et al. Colossal electroresistance and giant magnetoresistance in doped  $\text{PbPdO}_2$  thin films. *Adv Mater.* 2009;21(21):2196–2199. doi: [10.1002/adma.200802868](https://doi.org/10.1002/adma.200802868)
- [26] Choo SM, Lee KJ, Park SM, et al. Crossover between weak anti-localization and weak localization by co doping and annealing in gapless  $\text{PbPdO}_2$  and spin gapless co-doped  $\text{PbPdO}_2$ . *Appl Phys Lett.* 2015;106(17):172404. doi: [10.1063/1.4919452](https://doi.org/10.1063/1.4919452)
- [27] Yang Y, Zhang JM, Jia H, et al. Origin of the high-temperature ferromagnetism in Co-doped  $\text{PbPdO}_2$  semiconductors: a theoretical and experimental study. *J Appl Phys.* 2021;130(5):055705. doi: [10.1063/5.0057491](https://doi.org/10.1063/5.0057491)
- [28] Jia H, Chen Y, Lin C, et al. The novel positive colossal electroresistance in  $\text{PbPdO}_2$  thin film with (002) preferred orientation. *Ceram Int.* 2021;47(19):26768–26778. doi: [10.1016/j.ceramint.2021.06.085](https://doi.org/10.1016/j.ceramint.2021.06.085)
- [29] Ok JM, Brahlek M, Choi WS, et al. Pulsed-laser epitaxy of metallic delafossite  $\text{PdCrO}_2$  films. *APL Mater.* 2020;8(5):051104. doi: [10.1063/1.5144743](https://doi.org/10.1063/1.5144743)
- [30] Harada T, Fujiwara K, Tsukazaki A. Highly conductive  $\text{PdCoO}_2$  ultrathin films for transparent electrodes. *APL Mater.* 2018;6(4):046107. doi: [10.1063/1.5027579](https://doi.org/10.1063/1.5027579)
- [31] Hong D, Liu C, Wang L, et al. Coupling and decoupling of spin crossover and ferroelastic distortion: unsymmetric hysteresis loop, phase diagram, and sequence of phases. *Phys Rev Mater.* 2021;5(4):044205. doi: [10.1103/PhysRevMaterials.5.044205](https://doi.org/10.1103/PhysRevMaterials.5.044205)
- [32] Waser J, McClanahan ED. The crystal structure of  $\text{NaPt}_3\text{O}_4$ . *J Chem Phys.* 1951;19(4):413–416. doi: [10.1063/1.1748239](https://doi.org/10.1063/1.1748239)
- [33] Momma K, Izumi F. VESTA 3 for three-dimensional visualization of crystal, volumetric and morphology data. *J Appl Cryst.* 2011;44(6):1272–1276. doi: [10.1107/S0021889811038970](https://doi.org/10.1107/S0021889811038970)
- [34] Kresse G, Furthmüller J. Efficient iterative schemes for ab initio total-energy calculations using a plane-wave basis set. *Phys Rev B.* 1996;54(16):11169–11186. doi: [10.1103/physrevb.54.11169](https://doi.org/10.1103/physrevb.54.11169)
- [35] Kresse G, Joubert D. From ultrasoft pseudopotentials to the projector augmented-wave method. *Phys Rev B.* 1999;59(3):1758–1775. doi: [10.1103/PhysRevB.59.1758](https://doi.org/10.1103/PhysRevB.59.1758)
- [36] Heyd J, Scuseria GE, Ernzerhof M. Hybrid functionals based on a screened Coulomb potential. *J Chem Phys.* 2003;118(18):8207–8215. doi: [10.1063/1.1564060](https://doi.org/10.1063/1.1564060)
- [37] Heyd J, Scuseria GE, Ernzerhof M, et al. Erratum: Hybrid functionals based on a screened Coulomb potential [J. Chem. Phys. 118, 8207 (2003)]. *J Chem Phys.* 2006;124(21):219906. doi: [10.1063/1.1564060](https://doi.org/10.1063/1.1564060)
- [38] Krukau AV, Vydrov OA, Izmaylov AF, et al. Influence of the exchange screening parameter on the performance of screened hybrid functionals. *J Chem Phys.* 2006;125(22):224106. doi: [10.1063/1.2404663](https://doi.org/10.1063/1.2404663)
- [39] Nell J, O'Neill HSC. Gibbs free energy of formation and heat capacity of  $\text{PdO}$ : a new calibration of the  $\text{Pd}$ – $\text{PdO}$  buffer to high temperatures and pressures. *Geochim Cosmochim Acta.* 1996;60(14):2487–2493. doi: [10.1016/0016-7037\(96\)00115-9](https://doi.org/10.1016/0016-7037(96)00115-9)
- [40] Gorbenko OY, Samoilnikov SV, Graboy IE, et al. Epitaxial stabilization of oxides in thin films. *Chem Mater.* 2002;14(10):4026–4043. doi: [10.1021/cm021111v](https://doi.org/10.1021/cm021111v)
- [41] Doublet ML, Canadell E, Whangbo MH. Structure-property correlations in the platinum oxide and palladium sulfide bronzes with columnar chains of square-planar  $\text{TX}_4$  units ( $\text{T} = \text{Pt}$ ,  $\text{X} = \text{O}$ ;  $\text{T} = \text{Pd}$ ,  $\text{X} = \text{S}$ ). *J Am Chem Soc.* 1994;116(5):2115–2120. doi: [10.1021/ja00084a057](https://doi.org/10.1021/ja00084a057)
- [42] Aso R, Kan D, Shimakawa Y, et al. Atomic level observation of octahedral distortions at the perovskite oxide heterointerface. *Sci Rep.* 2013;3(1):2214. doi: [10.1038/srep02214](https://doi.org/10.1038/srep02214)
- [43] Li Z, Song D, Yu R, et al. Competing interfacial reconstruction mechanisms in  $\text{La}_{0.7}\text{Sr}_{0.3}\text{MnO}_3/\text{SrTiO}_3$  heterostructures. *ACS Appl Mater Interfaces.* 2016;8(36):24192–24197. doi: [10.1021/acsami.6b07569](https://doi.org/10.1021/acsami.6b07569)
- [44] Song K, Min T, Seo J, et al. Electronic and structural transitions of  $\text{LaAlO}_3/\text{SrTiO}_3$  heterostructure driven

- by polar field-assisted oxygen vacancy formation at the surface. *Adv Sci.* **2021**;8(14):2002073. doi: [10.1002/advs.202002073](https://doi.org/10.1002/advs.202002073)
- [45] Becke AD, Johnson ER. A simple effective potential for exchange. *J Chem Phys.* **2006**;124(22):221101. doi: [10.1063/1.2213970](https://doi.org/10.1063/1.2213970)
- [46] Tran F, Blaha P. Accurate band gaps of semiconductors and insulators with a semilocal exchange-correlation potential. *Phys Rev Lett.* **2009**;102(22):226401. doi: [10.1103/PhysRevLett.102.226401](https://doi.org/10.1103/PhysRevLett.102.226401)
- [47] Kazama K, Sakano M, Yamagami K, et al. Charge transport and thermopower in the electron-doped narrow gap semiconductor  $\text{Ca}_{1-x}\text{La}_x\text{Pd}_3\text{O}_4$ . *Phys Rev Mater.* **2023**;7(8):085402. doi: [10.1103/PhysRevMaterials.7.085402](https://doi.org/10.1103/PhysRevMaterials.7.085402)
- [48] Reddy BH, Al A, Singh RS. Electronic structure of ternary palladates and effect of hole doping: a valence band photoemission spectroscopic study. *J Phys Condens Mater.* **2021**;33(18):185502. doi: [10.1088/1361-648X/abf0c7](https://doi.org/10.1088/1361-648X/abf0c7)